forests

MDPI

Article

Estimation of Leaf Area Index for *Dendrocalamus giganteus* Based on Multi-Source Remote Sensing Data

Zhen Qin [1], Huanfen Yang [1], Qingtai Shu [1,*], Jinge Yu [2], Li Xu [1], Mingxing Wang [1], Cuifen Xia [1] and Dandan Duan [3]

[1] College of Forestry, Southwest Forestry University, Kunming 650224, China; qz5934578@swfu.edu.cn (Z.Q.); yanghf@swfu.edu.cn (H.Y.); xl15121267342@swfu.edu.cn (L.X.); wmxing7@swfu.edu.cn (M.W.); xcf@swfu.edu.cn (C.X.)
[2] School of Ecology and Applied Meteorology, Nanjing University of Information Science & Technology, Nanjing 210044, China; yjg721@swfu.edu.cn
[3] Information Technology Research Center, Beijing Academy of Agriculture and Forestry Sciences, Beijing 100097, China; duandd@nercita.org.cn
* Correspondence: shuqt@swfu.edu.cn; Tel.: +86-130-0869-3168

Abstract: The Leaf Area Index (LAI) plays a crucial role in assessing the health of forest ecosystems. This study utilized ICESat-2/ATLAS as the primary information source, integrating 51 measured sample datasets, and employed the Sequential Gaussian Conditional Simulation (SGCS) method to derive surface grid information for the study area. The backscattering coefficient and texture feature factor from Sentinel-1, as well as the spectral band and vegetation index factors from Sentinel-2, were integrated. The random forest (RF), gradient-boosted regression tree (GBRT) model, and K-nearest neighbor (KNN) method were employed to construct the LAI estimation model. The optimal model, RF, was selected to conduct accuracy analysis of various remote sensing data combinations. The spatial distribution map of *Dendrocalamus giganteus* in Xinping County was then generated using the optimal combination model. The findings reveal the following: (1) Four key parameters—optimal fitted segmented terrain height, interpolated terrain surface height, absolute mean canopy height, and solar elevation angle—are significantly correlated. (2) The RF model constructed using a combination of ICESat-2/ATLAS, Sentinel-1, and Sentinel-2 data achieved optimal accuracy, with a coefficient of determination (R^2) of 0.904, root mean square error (RMSE) of 0.384, mean absolute error (MAE) of 0.319, overall estimation accuracy (P_1) of 88.96%, and relative root mean square error (RRMSE) of 11.04%. (3) The accuracy of LAI estimation using a combination of ICESat-2/ATLAS, Sentinel-1, and Sentinel-2 remote sensing data showed slight improvement compared to using either ICESat-2/ATLAS data combined with Sentinel-1 or Sentinel-2 data alone, with a significant enhancement in LAI estimation accuracy compared to using ICESat-2/ATLAS data alone. (4) LAI values in the study area ranged mainly from 2.29 to 2.51, averaging 2.4. Research indicates that employing ICESat-2/ATLAS spaceborne LiDAR data for regional-scale LAI estimation presents clear advantages. Incorporating SAR data and optical imagery and utilizing diverse data types for complementary information significantly enhances the accuracy of LAI estimation, demonstrating the feasibility of LAI inversion with multi-source remote sensing data. This approach offers an innovative framework for utilizing multi-source remote sensing data for regional-scale LAI inversion, demonstrates a methodology for integrating various remote sensing data, and serves as a reference for low-cost high-precision regional-scale LAI estimation.

Keywords: ICESat-2/ATLAS; multi-source remote sensing data; Sequential Gaussian Conditional Simulation; Leaf Area Index; inversion

check for updates

Citation: Qin, Z.; Yang, H.; Shu, Q.; Yu, J.; Xu, L.; Wang, M.; Xia, C.; Duan, D. Estimation of Leaf Area Index for *Dendrocalamus giganteus* Based on Multi-Source Remote Sensing Data. *Forests* **2024**, *15*, 1257. https://doi.org/10.3390/f15071257

Academic Editors: Huaiqing Zhang, Juan Suárez-Minguez, Qi Chen, Yunsheng Wang, Safa Tharib, Hua Sun, Weipeng Jing, Huaguo Huang, Ting Yun and Meili Wang

Received: 25 June 2024
Revised: 9 July 2024
Accepted: 18 July 2024
Published: 19 July 2024

Copyright: © 2024 by the authors. Licensee MDPI, Basel, Switzerland. This article is an open access article distributed under the terms and conditions of the Creative Commons Attribution (CC BY) license (https://creativecommons.org/licenses/by/4.0/).

1. Introduction

The Leaf Area Index (LAI) represents the total sum of single-sided leaf area per unit of ground surface area, thus characterizing the size of the leaf area per unit area within an

ecosystem. It serves as a crucial parameter for reflecting vegetation structural characteristics and for simulating terrestrial ecological processes, water cycling, and biogeochemical cycling. Given that leaf surfaces are primary sites for material and energy exchange, important biophysical processes such as canopy interception, evapotranspiration, and photosynthesis are closely associated with LAI [1]. The LAI is a dimensionless parameter, exhibiting substantial variations across growth environments, plant species characteristics, leaf shapes, and features. This parameter correlates with a multitude of factors such as vegetation type, growth cycle, leaf inclination angle, leaf cluster characteristics, and non-foliar biomass, being influenced by measurement techniques. Furthermore, it contributes to assessing vegetation coverage and ecosystem health, thereby furnishing a scientific foundation for ecological environmental management [2]. Hence, the scientific and efficient acquisition of spatial distribution information regarding vegetation LAI on a large scale has long been a focal point of research in forestry. Direct LAI measurement methods, capable of achieving high measurement accuracy, are hindered by their time-consuming and costly nature, and are limited to point scales. These inherent limitations make obtaining spatial distribution information on large-scale LAI challenging, thereby hindering their practical applications. In contrast to direct LAI measurement methods, indirect LAI measurement methods are typically faster, more cost-effective, and have broader coverage. Moreover, regular acquisition of remote sensing data allows for long-term LAI monitoring [3].

In recent years, owing to the rapid advancement in satellite remote sensing technology, Light Detection and Ranging (LiDAR), microwave remote sensing, and optical remote sensing have found extensive applications in the estimation of forest structural parameters. The LIDAR operates by emitting laser pulses and measuring the time it takes for these pulses to reflect back to the sensor from the target, a process known as time-of-flight. By calculating the time-of-flight, three-dimensional images of the target were generated and highly accurate data were obtained. Optical remote sensing data can furnish information about the horizontal canopy structure, whereas microwave remote sensing and LiDAR can provide data concerning the vertical forest structure. Although optical remote sensing effectively mitigates the drawbacks of traditional techniques, it also possesses certain limitations. Optical remote sensing, akin to microwave remote sensing, is vulnerable to terrain effects, and may confront spectral signal saturation issues at the regional scale [4]. Airborne LiDAR, as an advanced remote sensing technology, possesses the capability to acquire vegetation structure information at various heights with high precision, thus facilitating accurate LAI inversion. However, the high cost of equipment and data acquisition, coupled with the collection of strip-shaped data primarily within a limited range, serve as limiting factors to the widespread promotion and application of this technology [5]. Synthetic Aperture Radar (SAR) possesses the advantage of being impervious to meteorological conditions, facilitating the all-weather modeling of vegetation LAI. Nonetheless, the precision of models derived from this technology is subject to the influence of diverse factors, encompassing sensor characteristics, canopy structure, and surface properties, thereby partially constraining its extensive application [6].

Spaceborne LiDAR, as an innovative active sensing technology, integrates a variety of existing techniques, thereby providing higher resolution and precision. It can accurately capture surface structures and their changes, effectively addressing the issue of "saturation" encountered in traditional optical imagery. Consequently, it enables the precise acquisition of detailed parameter information for the study subjects [7]. The spaceborne LiDAR ICESat-2 (Ice, Cloud, and Land Elevation Satellite-2)/ATLAS (Advanced Topographic Laser Altimeter System), launched on 15 September 2018, inherited and developed the technical advantages of ICESat (Ice, Cloud, and Land Elevation Satellite)/GLAS (Geoscience Laser Altimetry System). Furthermore, ATLAS utilized single-photon detection technology, enabling it to provide higher ground vertical resolution and elevation measurement accuracy, as well as offering a wider measurement range and improved resolution [8]. Spaceborne LiDAR data from ICESat-2/ATLAS are currently extensively utilized in polar ice sheets, sea ice, and forest vegetation, facilitating high-precision elevation measurements and data

monitoring [9]. In forestry applications, these data are primarily utilized to monitor canopy height at a regional scale, as well as to estimate and invert biomass and carbon storage [10]. With the continuous advancement of remote sensing technology, spaceborne LiDAR has gradually found application in the efficient and large-scale retrieval of forest structural parameters. However, despite these advancements, there exists limited research on estimating forest LAI utilizing spaceborne LiDAR, necessitating further exploration to evaluate the effectiveness and accuracy of this technology in assessing forest LAI [11]. Considering the substantial impact of complex terrain on the data quality of optical and microwave remote sensing imagery, as well as the relatively discrete footprint of spaceborne LiDAR, the uncertainty introduced by a single remote sensing data source in LAI estimation is considerable. Consequently, scholars tend to integrate multiple remote sensing data sources to enhance the accuracy of LAI estimation and effectively address the limitations of individual data sources.

Dendrocalamus giganteus, renowned for its towering and sturdy culms as well as its diverse applications, has emerged as a significant economic crop in the Yunnan region, owing to its exceptional environmental adaptability and rapid growth rate. In the southeastern to southwestern regions of Yunnan, *Dendrocalamus giganteus* is extensively distributed, with culms typically ranging in height from 20 to 30 m and diameters reaching 20 to 30 cm. Highly favored in interior design and decoration, it is commonly employed in the manufacture of furniture, decorative items, and various construction materials. Due to its robust material and substantial size, *Dendrocalamus giganteus* is also frequently employed as a building material and in wickerwork, making it suitable for constructing large-scale structures and intricate weaving products. Furthermore, with the growing demand for green and sustainable materials, *Dendrocalamus giganteus* is garnering increased attention due to its capacity for carbon sequestration and environmentally friendly characteristics [12]. Therefore, promoting the development of the *Dendrocalamus giganteus* industry not only contributes to increasing the income of local bamboo farmers and stimulating economic growth, but also contributes to environmental protection and sustainable development.

Current research on the LAI predominantly centers on forests, with a paucity of studies investigating bamboo forests, especially the LAI of *Dendrocalamus giganteus*. Hence, the utilization of remote sensing technologies like ICESat-2/ATLAS to estimate the LAI of *Dendrocalamus giganteus* shows promising potential [13]. Although many studies employ remote sensing techniques to estimate vegetation LAI, the majority rely on a singular remote sensing data source [14]. Studies that integrate ICESat-2/ATLAS with other remote sensing data for regional-scale LAI estimation of *Dendrocalamus giganteus* are rare. In this investigation, the Sequential Gaussian Conditional Simulation method was utilized, amalgamating ICESat-2/ATLAS photon data with various remote sensing datasets. By employing RF, GBRT, and KNN models, we crafted an optimal LAI estimation model and delved into the optimal combination of multi-source remote sensing data for LAI inversion. The effectiveness and feasibility of regional-scale LAI estimation for *Dendrocalamus giganteus* in Xinping County were analyzed. This study presents a pivotal case study in advocating for the sustainable development of bamboo forestry in China, and augments research on quantifying carbon sequestration in both forests and bamboo forests. This endeavor holds immense significance in advancing scientific and technological innovation within bamboo forestry and enhancing the economic value of bamboo forests alongside their environmental service functions.

2. Materials and Methods

2.1. Study Area

Yuxi City, located in Yunnan Province, encompasses Xinping County (Xinping Yi and Dai Autonomous County), situated between 23°38′ to 24°26′ N and 101°16′ to 102°16′ E. Situated in the southwestern region of Yunnan Province, Xinping County falls under the administrative authority of Yuxi City, encompassing a total land area of 4223 km^2, constituting 27.6% of Yuxi City's entire territory. The Yuanjiang River traverses Xinping County

along the Ailao Mountain range, demarcating the county into two distinct regions. Xinping County boasts a plateau terrain characterized by elevated landscapes in the northwest and lower elevations in the southeast. Damaoyan Peak, the primary summit of the Ailao Mountain, stands as the highest elevation in the county, towering at 3165.9 m, while the lowest point lies within the Nanhao Group, Mosha Town, at an elevation of 422 m. The yearly mean temperature registers at 18.1 °C, accompanied by an annual precipitation of 869 mm [15]. Figure 1 offers geographical location data for Xinping County. *Dendrocalamus giganteus* exhibits wide distribution across Xinping County. Renowned for its resilience to drought and barren conditions, it flourishes in warm climates, but is sensitive to cold temperatures. Optimal growth conditions for *Dendrocalamus giganteus* necessitate an average annual temperature of at least 17 °C, with an annual accumulated temperature exceeding 5500 °C. *Dendrocalamus giganteus* holds dual significance as both an ornamental and a distinctive material bamboo species. *Dendrocalamus giganteus* plays a pivotal role in stimulating economic development and has become an integral component of local livelihoods, thereby elevating the bamboo industry to a position of prominence within Xinping County. Hence, precise and efficient estimation and analysis of *Dendrocalamus giganteus'* LAI are instrumental in fostering rural revitalization and optimizing agricultural structural enhancements. Additionally, it serves as a catalyst for agricultural technological innovation.

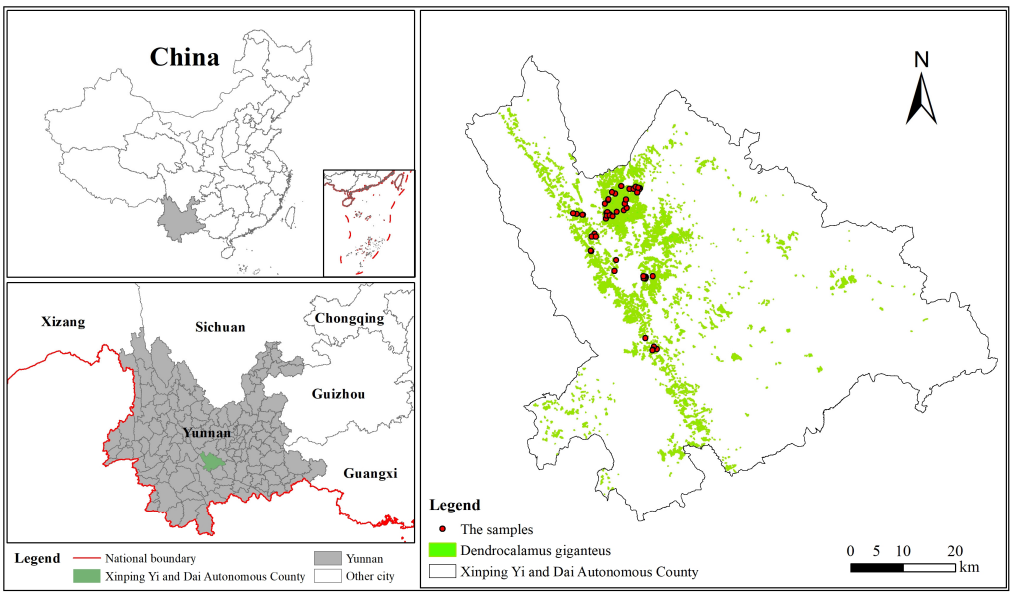

Figure 1. Location of Xinping Yi and Dai Autonomous County. Note: The base map in this figure is named "Administrative Map of Yunnan Province", with the review number Yun S (2020) No. 102. It was supervised by the Yunnan Provincial Department of Natural Resources and produced by the Yunnan Provincial Map Institute. The same applies below.

2.2. Datasets and Preprocessing

2.2.1. Ground Survey Data Collection and Processing

For this study, drawing upon the results of the forest resource planning and design survey conducted in Yunnan Province, 51 circular plots with a radius of 8.5 m were established in Xinping County, Yuxi City, Yunnan Province, on 8 January 2024, as depicted in Figure 1. In this study, we employed the Thousand Vision Star Matrix SR3 (Pro version) differential positioning instrument (SR3, Pro version, Chengdu, Sichuan, China) to collect the coordinates of the circular plots in a fixed solution state, thereby ensuring the accuracy of the plot coordinates. Advanced hemispherical photography was employed in this study to accurately capture LAI data measured in the field [16]. Nine shooting points were uniformly selected within each plot to ensure the comprehensive coverage of various vegetation. Subsequently, precise shooting was conducted at each point using a fisheye

lens to ensure the capture of fisheye photos encompassing the canopy distribution areas. Consequently, nine fisheye photos were obtained within each plot. To ensure measurement accuracy, appropriate lighting conditions must be maintained within the selected plots. During the shooting process, direct exposure to sunlight should be minimized to avoid inaccuracies in reflecting the true condition of the samples. Subsequently, preprocessing was performed on the fisheye photos from the 51 plots that met the standards. To ensure the accuracy and consistency of the image data, the aspect ratio of all photos was initially adjusted to the standard size of 3000 × 4000 pixels and uniformly converted to JPG format. Subsequently, they were imported into CANEYE (CANEYE, version 6.495, INRA, Paris, France), a hemispherical image analysis software developed based on MATLAB (MATLAB, version R2018a, Natick, MA, USA) programming, where relevant parameters were adjusted accordingly. Following analysis, the measured LAI values of the 51 *Dendrocalamus giganteus* plots were determined. The descriptive statistical characteristics of the measured LAI in the sample plots are depicted in Table 1.

Table 1. Descriptive statistics of measured LAI in effective sample plots.

Sample Size	Minimum Value	Maximum Value	Mean Value	Standard Deviation	Variance
51	1.31	4.98	3.43	0.94	0.89

2.2.2. ICESat-2/ATLAS Data

The ICESat-2 is equipped with the Advanced Topographic Laser Altimetry System (ATLAS), which employs the principle of photon round-trip time for ranging. ATLAS utilizes single-photon detection technology to emit 532 nm green laser pulses at a frequency of 10 kHz. Each laser pulse contains over 100 trillion photons. These pulses are split into 3 pairs of 6 beams using a spectroscope, enabling the acquisition of photon point cloud data with a diameter of approximately 17 m and an along-track distance of 0.7 m. Each pair of beams consists of a strong beam and a weak beam, with an energy ratio of approximately 4:1. The two beams are spaced approximately 90 m apart vertically, and the separation between different pairs of beams along the orbit is about 3.3 km [17]. This study employed Level-2 (ATL03) and Level-3A (ATL08) data products obtained from ICESat-2/ATLAS. The ATL08 product is derived from ATL03 data using the DRAGANN (Gaussian adaptive nearest neighbor) denoising algorithm and an improved Progressive Triangular Irregular Network Densification (PTD) classification method, providing various parameter information regarding the vegetation canopy and terrain [18]. Comprehensive descriptions of the ICE-Sat-2 data products can be accessed at https://nsidc.org/data/ICESat-2/datasets (accessed on 15 January 2024). This study obtained all accessible ATL03 and ATL08 data products encompassing the study area from January 2022 to August 2023. The ATL03 data consist of 44 records, encompassing 132 orbits and 264 beams, whereas the ATL08 data comprise 44 records, covering 132 orbits and 264 beams. The ICESat-2/ATLAS data utilized in this study are openly accessible for downloading from the Earthdata website (https://search.earthdata.nasa.gov/, accessed on 15 January 2024).

2.2.3. Sentinel-1/-2 Data

Sentinel-1 is a high-resolution synthetic aperture radar (SAR) satellite. Sentinel-1A was successfully launched on 3 April 2014, and Sentinel-1B followed suit on 25 April 2016. Both satellites have a revisit period of 12 days and carry sensors based on C-band SAR technology. Positioned 180 degrees apart on the same orbital plane, these two satellites ensure optimal global coverage and facilitate data transmission. They provide data in four polarization modes—Vertically Transmit, Vertically Receive (VV), Vertically Transmit, Horizontally Receive (VH), Horizontally Transmit, Horizontally Receive (HH), and Horizontally Transmit, Vertically Receive (HV)—with a resolution of 10 m [19]. With all-weather imaging capabilities, Sentinel-2 satellites provide high-resolution and medium-resolution measurement data for land, coastal, and ice areas. Sentinel-2 satellites are high-resolution

multispectral imaging satellites, consisting of Sentinel-2A and Sentinel-2B. Each satellite has a revisit period of 10 days, and the two satellites complement each other to achieve a combined revisit period of 5 days. Sentinel-2A was successfully launched on 23 June 2015, followed by the launch of Sentinel-2B on 7 March 2017. They are primarily used for global land observation, covering land vegetation, soil, water resources, inland waterways, and coastal areas. The Sentinel-2 satellite carries a Multi-Spectral Instrument (MSI), and orbits at an altitude of 786 km. It covers 13 spectral bands with a swath width of 290 km. The spectral range spans from visible light to near-infrared and short-wave infrared. Bands B2 (Blue, 458–523 nm), B3 (Green, 543–578 nm), B4 (Red, 650–680 nm), and B8 [Near Infrared (NIR), 785–899 nm] have a resolution of 10 m, while bands B5 (Vegetation Red Edge, 698–712 nm), B6 (Vegetation Red Edge, 732–748 nm), B7 (Vegetation Red Edge, 773–793 nm), B8A (Vegetation Red Edge, 855–875 nm), B11 (SWIR, 1560–1660 nm), and B12 (SWIR, 2100–2300 nm) have a resolution of 20 m, and bands B1 (Coastal Aerosol, 443–453 nm), B9 (Water Vapor, 940–960 nm), and B10 (SWIR-Cirrus, 1360–1390 nm) have a resolution of 60 m [20]. These data provide valuable information on land vegetation growth, soil cover conditions, and environmental aspects of inland and coastal areas [21]. This study obtained Sentinel-1/-2 images from October 2023, which are freely available for download through the Google Earth Engine (GEE) platform (https://earthengine.google.com/, accessed on 15 January 2024).

3. Research Methods and Data Processing

3.1. Research Methodology

In this study, we initially employed the Sequential Gaussian Conditional Simulation (SGCS) method, rooted in simple kriging, to interpolate the footprint parameters furnished using ICESat-2/ATLAS, thus acquiring surface information. Following that, multiple remote sensing images were harmonized with ICESat-2/ATLAS parameters to scrutinize the correlation between each variable and LAI. Various combinations of remote sensing data sources were subsequently utilized, leading to the development of LAI estimation models using Random Forest (RF), Gradient-Boosting Regression Trees (GBRT), and K-Nearest Neighbors (KNN) methods. The spatial distribution map of regional-scale *Dendrocalamus giganteus* LAI is derived by employing the optimal remote sensing data combination model. The technical approach of this study is delineated in Figure 2.

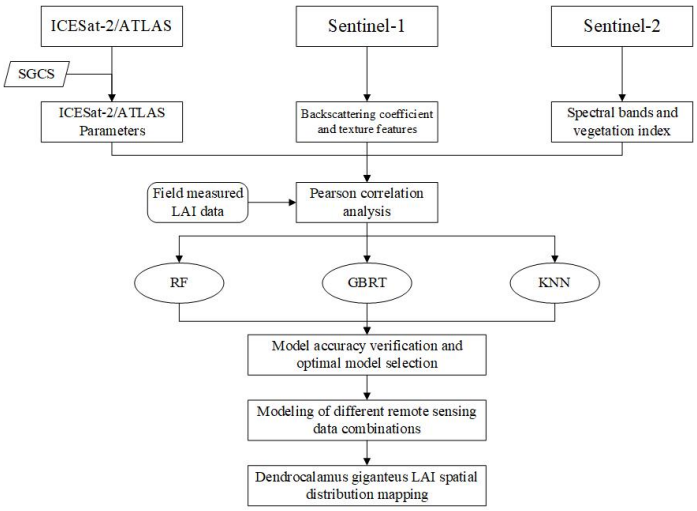

Figure 2. Technology roadmap.

3.1.1. Sequential Gaussian Conditional Simulation

- Feature variable normalization

In order to expedite model convergence, prior to conducting variance function analysis, all variables undergo normalization to scale their values within the range of [0, 1] or [−1, 1].

Subsequently, the data structure of each variable undergoes a normality test, and variables showing nonnormal distributions are subjected to cube root transformation to approximate a normal distribution. This process facilitates the subsequent variance function analysis. The calculation formula is as follows:

$$Y = \frac{y - y_{min}}{y_{max} - y_{min}} \quad (1)$$

Note: Y represents the result of normalization processing; y represents the initial value; y_{min} represents the minimum value of the initial data; and y_{max} represents the maximum value of the initial data.

- Variance function

The Variance Function, often referred to as the semivariance function, plays a pivotal role in kriging interpolation, serving as a fundamental analytical instrument in spatial statistics. It characterizes the spatial distribution pattern of regionalized variables, and offers a quantitative depiction of the spatial autocorrelation within geographic data. The experimental variogram derived from variogram computation requires fitting using methodologies like the spherical model, exponential model, linear model, and Gaussian model to develop its theoretical variogram function model, thus furnishing a theoretical underpinning for the structural analysis of geoscientific variables and their spatial local estimation, specifically kriging interpolation [22]. The structural attributes of its theoretical model are delineated by four parameters: function type, nugget variance (C_0), sill (C_0 + C, where C represents the partial sill), and range (a). The functional expression is provided below:

$$\gamma(h) = \frac{1}{2n(h)} \sum_{i=1}^{n(h)} [Z(X_i) - Z(X_i + h)]^2 \quad (2)$$

Note: $\gamma(h)$ represents the variogram function; h represents the sampling interval between paired sample points; $n(h)$ represents the total number of paired samples when the spacing between sample points is h; and $Z(X_i)$ and $Z(X_i + h)$ represent the attribute values of the regionalized variable at spatial locations X_i and $X_i + h$, respectively.

- Principle of Sequential Gaussian Conditional Simulation

Geostatistics plays a crucial role in the analysis of forest spatial structures and parameter estimation [23]. Sequential Gaussian Conditional Simulation, based on the Monte Carlo method, is a spatial stochastic simulation technique that performs well in estimating vegetation structural parameters over large regions [24]. Widely applied in geosciences, geostatistics serves to quantify the uncertainty of regionalized attributes [25]. Sequential Gaussian Conditional Simulation constructs Gaussian functions utilizing existing data, and considers the values of the regional-scale random variable $Z(x)$ as random realizations of the normal distribution function $F(x)$. At each simulation location x_m, known data $Z(x_i)$ (i = 1, 2, …, n) and previously simulated values $Z(x_j)$ (j = 1, 2, …, $m - 1$) are used to derive the conditional cumulative probability density function $F(x)$. Subsequently, spatial predictions are generated through random simulation by employing the cumulative conditional probability distribution [26]. The Kriging interpolation method, widely utilized in forestry, is distinguished by its impartiality and minimal estimation error variance [27]. Nonetheless, minimizing error variance may induce a smoothing effect [28], potentially leading to a biased estimation of global spatial variability. Thus, the primary application of this method is for local estimation. In contrast to the Kriging interpolation method, Sequential Gaussian Conditional Simulation employs the Monte Carlo method to derive the probability density function based on the original data. The variance of simulated values at any given point equals the variance of the Gaussian distribution of the original data, thus circumventing the smoothing effect [29,30], an inherent trait of all minimum mean squared error spatial estimators [31]. Sequential Gaussian Conditional Simulation can preserve the overall spatial variation intensity and generate multiple equally probable

realizations at each unsampled spatial location, thereby quantifying the spatial uncertainty of geographic attribute variation [32]. Since the collected data often fail to fully meet the simulation requirements, it is necessary to first normalize them and subsequently achieve the transformation of simulation results through inverse transformation [33].

3.1.2. LAI Estimation Model

- Random Forest

Random Forest (RF) represents an implementation of the Bagging method in ensemble learning [34]. It comprises multiple decision trees, and is constructed by utilizing various subsets of the training data and feature attributes. Upon inputting the training data into the model, RF does not construct a single large decision tree using the entire training dataset; rather, it builds multiple small decision trees from different subsets of data and features, subsequently combining them into a more robust model. Each subset is created by randomly selecting samples and features, with the aim of reducing the sensitivity of decision trees to the training data and preventing overfitting [35]. Through combining results from multiple decision trees, RF enhances model effectiveness, demonstrating high accuracy, robustness against noise and outliers, and computational efficiency advantages. However, it incurs significant memory usage and slower training speeds when dealing with large numbers of trees or datasets. The RF model was constructed utilizing the "randomForest" package within the R statistical program (RStudio, version 4.2.2, Boston, MA, USA) for this study.

- Gradient-Boosting Regression Trees

Gradient-Boosting Regression Trees (GBRT) constitute a distinct ensemble method divergent from random forests, distinguished by its focus on correction and enhancement. By combining multiple decision trees [36], it constructs a more robust model. The GBRT model serves as a function space optimization algorithm, capable of accommodating intricate nonlinear relationships. After each iteration, GBRT generates a weak learner with low accuracy; however, these learners are interdependent. The final ensemble achieves higher accuracy by integrating these weak learners [37]. GBRT could handle diverse data types, offering high predictive accuracy and robust anti-overfitting capabilities. However, configuring its parameters was complex, incurring high computational costs and rendering it unsuitable for real-time predictions. In this study, the GBRT model was implemented through the utilization of the "gbm" package in the R statistical program (RStudio, version 4.2.2, Boston, MA, USA).

- K-Nearest Neighbors

The K-Nearest Neighbors (KNN) algorithm, commonly employed in machine learning, operates on the principle of leveraging distance information to identify neighboring data points, subsequently determining the classification of the data point based on the class information of these neighbors. The KNN method, characterized by its simple structure, enables the simultaneous estimation of all variables. In contrast to univariate predictions, it better preserves the correlation and covariance structure among variables [38–40]. The KNN algorithm offers intuitive and easy-to-implement advantages; however, its efficiency and accuracy are constrained in large-scale high-dimensional datasets. In this study, we constructed the KNN model using the "kknn" package in the R statistical program (RStudio, version 4.2.2, Boston, MA, USA).

3.1.3. Evaluation of Model Accuracy

In this study, model accuracy is assessed utilizing the coefficient of determination (R^2), root mean square error (RMSE), mean absolute error (MAE), overall estimation accuracy (P_1), and relative root mean square error (RRMSE) [41]. A higher R^2 and P_1 value, closer to 1, indicates a better fit between predicted and observed values, whereas lower RMSE,

MAE, and RRMSE values, closer to 0, signify smaller errors in model estimation. The formulations for these statistical metrics are as follows:

$$R^2 = 1 - \frac{\sum_{i=1}^{n}(y_i - \hat{y}_i)^2}{\sum_{i=1}^{n}(y_i - \overline{y})^2} \quad (3)$$

$$RMSE = \sqrt{\frac{\sum_{i=1}^{n}(y_i - \hat{y}_i)^2}{n}} \quad (4)$$

$$MAE = \frac{1}{n}\sum_{i=1}^{n}|(y_i - \hat{y}_i)| \quad (5)$$

$$P_1 = \left(1 - \frac{RMSE}{\overline{y}}\right) \times 100\% \quad (6)$$

$$RRMSE = \frac{RMSE}{\frac{1}{n}\sum_{i=1}^{n}(y_i - \overline{y})^2} \quad (7)$$

Note: y_i represents the observed value; $\hat{y}_i$ denotes the estimated value; $\overline{y}$ represents the mean of estimated values; and n is the sample size.

3.2. Data Processing

3.2.1. Data Processing of ICESat-2/ATLAS

The acquisition of ATLAS photon data is influenced by multiple factors, including solar radiation, atmospheric scattering, terrain conditions, and sensor characteristics. In this study, we utilized a noise reduction algorithm based on an improved version of OPTICS to denoise ATL08 data within the study area, thereby effectively extracting the necessary signal photons. Following denoising processing, the ATLAS data contained signal photons, including those from vegetation canopies and surfaces. The denoised photon cloud data underwent processing using the enhanced Progressive Triangular Irregular Network Densification (PTD) method, resulting in the extraction of 21,080 valid footprints within the study area. Subsequently, a parameter extraction module for ICESat-2/ATLAS was developed using PyCharm IDL within a Python (Python, version 3.9, Amsterdam, The Netherlands) environment. The final distribution of ATLAS footprints within the study area is illustrated in Figure 3.

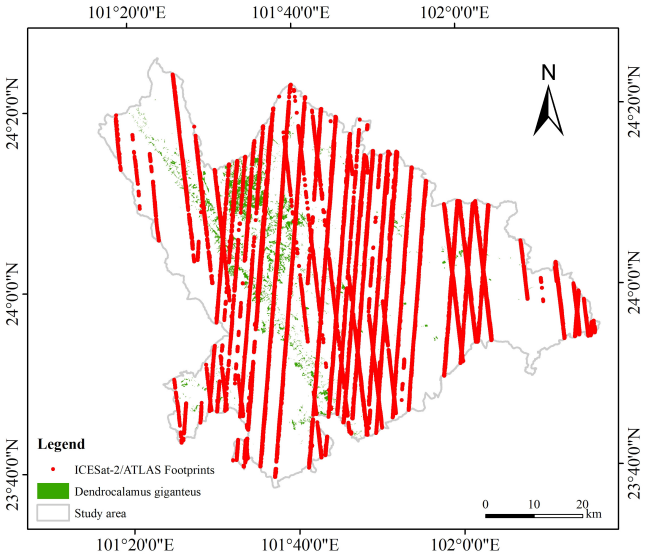

Figure 3. Light spot distribution map in the study area.

3.2.2. Data Processing of Sentinel-1/-2

In this study, we downloaded and pre-processed Sentinel-1 data using the Google Earth Engine (GEE) platform. The preprocessing steps included precise orbit correction, thermal noise removal, radiometric calibration, multi-looking, speckle filtering, geocoding, and decibel conversion. The spatial resolution was resampled to 15 m × 15 m. In ENVI (ENVI, version 5.3, Boulder, CO, USA) software, the second-order texture analysis method utilizing the Grey Level Co-occurrence Matrix (GLCM) was applied to generate texture images. The analysis employed a window size of 5 × 5, a step size of 1, and 64 gray levels, extracting eight pieces of texture feature information [42]. The study employed the Google Earth Engine (GEE) platform for downloading and preprocessing Sentinel-2 data. This process encompassed geographic registration, radiometric calibration, and atmospheric correction of Level-1C data to derive surface reflectance values. The spatial resolution was resampled to 15 m × 15 m. Subsequently, ENVI (ENVI, version 5.3, Boulder, CO, USA) software was utilized to extract image feature parameters, including spectral bands and vegetation indices.

3.2.3. Selection and Extraction of Feature Variables

- ICESat-2/ATLAS parameters

The ATL03 data product comprises geographic spatial location information for all photon events, encompassing time, latitude, longitude, altitude, and corrections to the geoid model. Each photon is indexed to concatenate all hierarchical data into a unified structure. The ATLAS data exhibit two types of single-photon indexing: one segment along-track distance, with each segment identified by a unique seven-digit number [43,44]. The ATL08 data product utilized in this study is generated via segment-based indexing. Derived from segmented ATL03 products, ATL08 data products offer a range of canopy and terrain-related indices. The ATL08 feature parameters employed in this study are listed in Table 2.

Table 2. ICESat-2/ATLAS characteristic factors.

Variable Factor Name	Meaning	Describe
solar_elevation	Solar elevation	Solar angle above or below the plane tangent to the ellipsoid surface at the laser spot.
h_mean_canopy_abs	Absolute mean canopy height	Mean of the individual absolute canopy heights within the segment referenced above the WGS84 Ellipsoid.
h_te_best_fit	Segment terrain height best fit	The best-fit terrain elevation at the mid-point location of each 100 m segment.
h_te_interp	Interpolated	Interpolated terrain surface height above the WGS84.

- Extraction of region-scale remote sensing data and feature variables

The optical remote sensing variables employed in this investigation comprised spectral indices, vegetation indices, and texture features. Vegetation indices prove effective in distinguishing vegetation from other land cover types, and serve as indicators reflecting plant growth conditions, canopy coverage, and biomass. They have been extensively applied in vegetation classification, environmental change monitoring, crop yield estimation, and various other domains [45]. Texture features elucidate the spatial distribution of brightness among neighboring pixels, thereby reflecting the appearance characteristics of objects, encompassing attributes such as color, texture, and shape [46]. This study extracted the backscattering coefficient and texture features from Sentinel-1 images (Table 3) and obtained original single spectral bands and vegetation indices (Table 4) from Sentinel-2 images. The extracted feature variables are displayed in Table 5.

Table 3. Calculation formula of the texture feature.

Texture Feature Parameter	Equation	Texture Feature Parameter	Equation
Mean (ME)	$ME = \sum_{i,j=0}^{n-1} iF_{i,j}$	Dissimilarity (DI)	$DI = \sum_{i,j=0}^{n-1} iF_{i,j}\left\|i-j\right\|$
Variance (VA)	$VA = \sum_{i,j=0}^{n-1} iF_{i,j}\left(i,j-\mu_{i,j}\right)^2$	Entropy (EN)	$EN = \sum_{i,j=0}^{n-1} iF_{i,j}\left\|-\ln F_{i,j}\right\|$
Homogeneity (HO)	$HO = \sum_{i,j=0}^{n-1} i\frac{F_{i,j}}{1+(i-j)^2}$	Second Moment (SM)	$SM = \sum_{i,j=0}^{n-1} iF_{i,j}^2$
Contrast (CO)	$CO = \sum_{i,j=0}^{n-1} iF_{i,j}(i-j)^2$	Correlation (CR)	$CR = \sum_{i,j=0}^{n-1} F_{i,j}\left[\frac{(i-\mu_i)\left(j-\mu_j\right)}{\sqrt{VA_iVA_j}}\right]$

Note: i represents the number of rows in GLCM, and j represents the number of columns, $F_{i,j}$ denotes the normalized element values of row i and column j in the normalized co-occurrence matrix, and $\mu_{i,j}$ represents the mean value of GLCM..

Table 4. Formula for calculating vegetation index.

Vegetation Index Name	Calculation Formula
Normalized Difference Vegetation Index (NDVI) [47]	$NDVI = \frac{B8-B4}{B8+B4}$
Difference Vegetation Index (DVI) [48]	$DVI = B8 - B4$
Soil-Adjusted Vegetation Index (SAVI) [49]	$SAVI = \frac{(B8-B4)(1+L)}{B8+B4+L}$
Optimized Soil-Adjusted Vegetation Index (OSAVI) [50]	$OSAVI = \frac{B8-B4}{B8+B4+0.16}$
Enhanced Vegetation Index (EVI) [51]	$EVI = 2.5 \times \frac{B8-B4}{B8+6B4-7.5B2+1}$
Two-band Enhanced Vegetation Index (EVI2) [52]	$EVI2 = 2.5\frac{B8-B4}{B8+B4+1}$
Ratio Vegetation Index (RVI) [53]	$RVI = \frac{B8}{B4}$
Modified Soil-Adjusted Vegetation Index (MSAVI) [54]	$MSAVI = \frac{2B8+1-\sqrt{(2B8+1)^2-8(B8-B4)}}{2}$
Green Normalized Difference Vegetation Index (GNDVI) [55]	$GNDVI = \frac{B8-B3}{B8+B3}$
Green Ratio Vegetation Index (GRVI) [56]	$GRVI = \frac{B3}{B4}$
Renormalized Difference Vegetation Index (RDVI) [56]	$RDVI = \frac{B8-B4}{\sqrt{B8+B4}}$
Infrared Difference Vegetation Index (IDVI) [57]	$IDVI = \frac{B8-B3}{B8+B3}$

Note: B2: Bands2, Blue; B3: Bands3, Green; B4: Bands4, Red; B8: Bands8, Near Infrared (NIR). The value of L is usually 0.5.

Table 5. Sentinel-1/2 variable factor extraction.

Data Source	Variable Type	Variable Name	Variables Number
Sentinel-1	Backscatter coefficient	VV, VH	2
	Texture features	VV-ME, VV-VA, VV-HO, VV-CO, VV-DI, VV-EN, VV-SM, VV-CR, VH-ME, VH-VA, VH-HO, VH-CO, VH-DI, VH-EN, VH-SM, VH-CR,	16
Sentinel-2	Original single spectral bands	B2, B3, B4, B5, B6, B7, B8, B8A	8
	Vegetation Index	NDVI, DVI, SAVI, OSAVI, EVI, EVI2, RVI, MSAVI, GNDVI, GRVI, RDVI, IDVI	12

Note: VV: Co-polarization; VH: Cross-polarization; VV-XX: Eight texture features of VV generated by Sentinel-1 using GLCM; VH-XX: Eight texture features of VH generated by Sentinel-1 using GLCM; ME: Mean; VA: Variance; HO: Homogeneity; CO: Contrast; DI: Dissimilarity; EN: Entropy; SM: Second Moment; CR: Correlation; B2: Bands2, Blue; B3: Bands3, Green; B4: Bands4, Red; B5: Bands5, Vegetation Red Edge; B6: Bands6, Vegetation Red Edge; B7: Bands7, Vegetation Red Edge; B8: Bands8, Near Infrared (NIR); B8A: Bands8A, Vegetation Red Edge.

4. Results and Analysis

4.1. Sequential Gaussian Condition Simulation Effect

4.1.1. Choice of Variance Function Model

This study utilized the GS+9.0 software to fit linear, spherical, exponential, and Gaussian models to the variogram functions, thereby selecting the optimal theoretical model. To ensure the accuracy of the models, in this study, we selected the optimal model based on criteria including the coefficient of determination (R^2), residual sum of squares (RSS), and the ratio of nugget variance to sill (variability).

The model parameters acquired via the GS+9.0 software are delineated in Table 6. The findings delineate the following outcomes: (1) The spherical model for parameters such as h_te_best_fit, h_te_interp, h_mean_canopy_abs, and solar_elevation demonstrated the highest R^2 and lowest RSS values, signifying optimal model performance. (2) The variation in h_te_best_fit, h_te_interp, and h_mean_canopy_abs surpassed 75%, implying a high degree of spatial autocorrelation for these variables, whereas the variability of solar_elevation fell between 25% and 75%, denoting moderate spatial autocorrelation for this factor. (3) h_te_best_fit manifested strong spatial autocorrelation within a radius of 27,500 m; h_te_interp showed strong spatial autocorrelation within a radius of 27,600 m; h_mean_canopy_abs displayed strong spatial autocorrelation within a radius of 27,800 m; and solar_elevation demonstrated moderate spatial autocorrelation within a radius of 13,000 m.

Table 6. Variation function analysis of characteristic factors.

Modeling Factors	Model	R^2	RSS	C_0	$C_0 + C$	$C_0/C_0 + C$/%	Range/m
h_te_best_fit	Linear	0.482	3.720	1.115120	2.736242	0.592	52,262.12
	Spherical	0.921	0.567	0.051000	2.397000	0.979	27,500.00
	Exponential	0.870	1.000	0.001000	2.465000	1.000	33,300.00
	Gaussian	0.914	0.618	0.314000	2.392000	0.869	22,516.66
h_te_interp	Linear	0.482	3.720	1.115268	2.736374	0.592	52,262.12
	Spherical	0.921	0.567	0.052000	2.398000	0.978	27,600.00
	Exponential	0.870	1.000	0.001000	2.465000	1.000	33,300.00
	Gaussian	0.914	0.618	0.319000	2.392000	0.867	22,516.66
h_mean_canopy_abs	Linear	0.492	2.740	1.074694	2.495106	0.569	52,262.12
	Spherical	0.925	0.406	0.163000	2.197000	0.926	27,800.00
	Exponential	0.877	0.687	0.001000	2.249000	1.000	31,800.00
	Gaussian	0.917	0.447	0.394000	2.192000	0.820	22,689.87
solar_elevation	Linear	0.254	1.214000	1741.631	2302.117	0.243	52,262.12
	Spherical	0.740	4.24100	710.0000	2151.000	0.670	13,000.00
	Exponential	0.690	5.04300	259.0000	2152.000	0.880	11,700.00
	Gaussian	0.732	4.35900	947.0000	2151.000	0.560	11,085.13

4.1.2. Sequential Gaussian Condition Simulation of LAI Model Spot Feature Factors

The LAI of *Dendrocalamus giganteus* underwent analysis through Sequential Gaussian Conditional Simulation (SGCS), employing Geostatistics software for environmental sciences (GS+, version 9.0, Plainwell, MI, USA) and ArcGIS (ArcGIS, version 10.8, Redlands, CA, USA) software. Initially, a variogram analysis was performed utilizing Geostatistics software for environmental sciences software to ascertain parameters such as the range and nugget variance of the optimal variogram model. Subsequently, simple kriging interpolation was executed, employing ArcGIS (ArcGIS, version 10.8, Redlands, CA, USA) software, relying on the parameters derived from the optimal variogram model. Gaussian geostatistical simulation (SGCS) analysis was subsequently conducted utilizing the Gaussian geostatistical simulation tool [58]. Multiple simulation runs were established, encompassing 1, 10, 25, 50, 75, and 100 iterations, aiming to ascertain the optimal number of simulations [33]. Experimental results suggest that as the number of SGCS simulations increases, the variance of *Dendrocalamus giganteus* LAI at the pixel level becomes more pronounced. However, once the number of SGCS simulations reaches 25, the coefficient of

variation begins to stabilize. Therefore, in this study, we decided to set the threshold for the number of simulations at 25. The effect of SGCS is depicted in Figure 4.

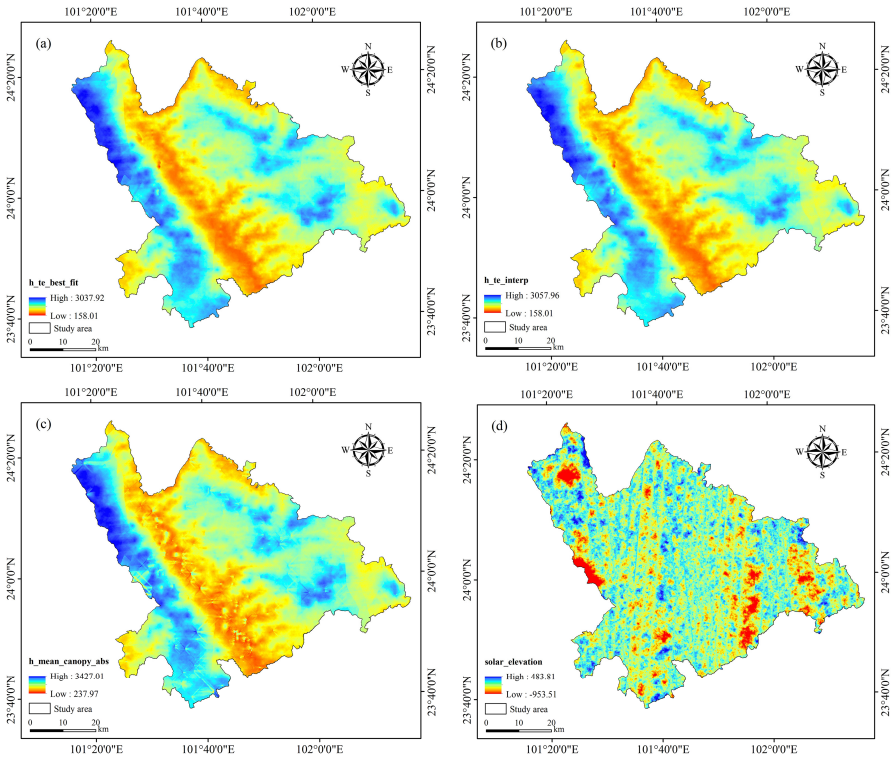

Figure 4. SGCS effect: (**a**) h_te_best_fit; (**b**) h_te_interp; (**c**) h_mean_canopy_abs; and (**d**) solar_elevation.

4.2. Variables Correlation Analysis

The study meticulously curated a comprehensive set of 84 model feature variables, comprising 46 ICESat-2/ATLAS feature parameters, 2 backscatter coefficients, and 16 texture feature factors extracted from Sentinel-1 data, alongside 8 single spectral bands and 12 vegetation index factors derived from Sentinel-2 observations. The Pearson correlation coefficient method was meticulously applied to identify variables significantly correlated with *Dendrocalamus giganteus* LAI at significance levels of 0.01, 0.05, and 0.1, respectively. The correlation matrix illustrating the significant correlations among variables is depicted in Figure 5. As depicted in Table 7, the Pearson correlation coefficients between remote sensing variables and LAI, at the 0.01 significance level, span from −0.384 to 0.367, encompassing VV_Mean and VV_Dissimilarity. At the 0.05 significance level, correlation coefficients vary from −0.336 to 0.352, encompassing h_te_best_fit, VV, VV_SecondMoment, VV_Homogeneity, VV_Entropy, VH_Mean, VH_Homogeneity, EVI, EVI2, IDVI, NDVI, OSAVI, RDVI, RVI, and SAVI. At the 0.1 significance level, correlation coefficients range from −0.236 to 0.271, including h_te_interp, solar_elevation, h_mean_canopy_abs, DVI, and MSAVI.

4.3. Estimation Results of Dendrocalamus giganteus LAI Model

Utilizing data acquired from spaceborne lidar ICESat-2/ATLAS, synthetic aperture radar Sentinel-1, and optical remote sensing imagery Sentinel-2, this investigation extracted pertinent feature factors. Employing a Pearson correlation analysis, select variables with high correlation were used as modeling factors. These variables encompass h_te_best_fit, h_te_interp, h_mean_canopy_abs, solar_elevation, VV_Mean, VV_Dissimilarity, EVI2, and NDVI. These factors, sourced from three distinct data reservoirs, were employed to construct a predictive LAI model, employing methodologies such as random forest,

gradient-boosting regression trees, and K-nearest neighbors. The accuracy of the model was evaluated utilizing metrics such as coefficient of determination (R^2), root mean square error (RMSE), mean absolute error (MAE), overall estimation accuracy (P_1), and relative root mean square error (RRMSE), delineated in Figure 6.

Table 7. Feature parameter correlation data Table.

Data Source	Parameters and Correlations
ICESat-2/ATLAS	h_te_best_fit (0.298) **, h_te_interp (0.271) *, solar_elevation (−0.236) *, h_mean_canopy_abs (0.248) *
Sentinel-1	VV_Mean (0.367) ***, VV_Dissimilarity (−0.384) ***, VV (0.315) **, VV_SecondMoment (0.336) **, VV_Homogeneity (0.324) **, VV_Entropy (−0.336) **, VH_Mean (0.329) **, VH_Homogeneity (0.352) **
Sentinel-2	EVI (0.319) **, EVI2 (0.343) **, NDVI (0.341) **, IDVI (0.341) **, OSAVI (0.341) **, RDVI (0.341) **, RVI (0.31) **, SAVI (0.341) **, DVI (0.252) *, MSAVI (0.243) *

Note: *** denotes a significance level of 0.01, ** denotes a significance level of 0.05, * denotes a significance level of 0.1

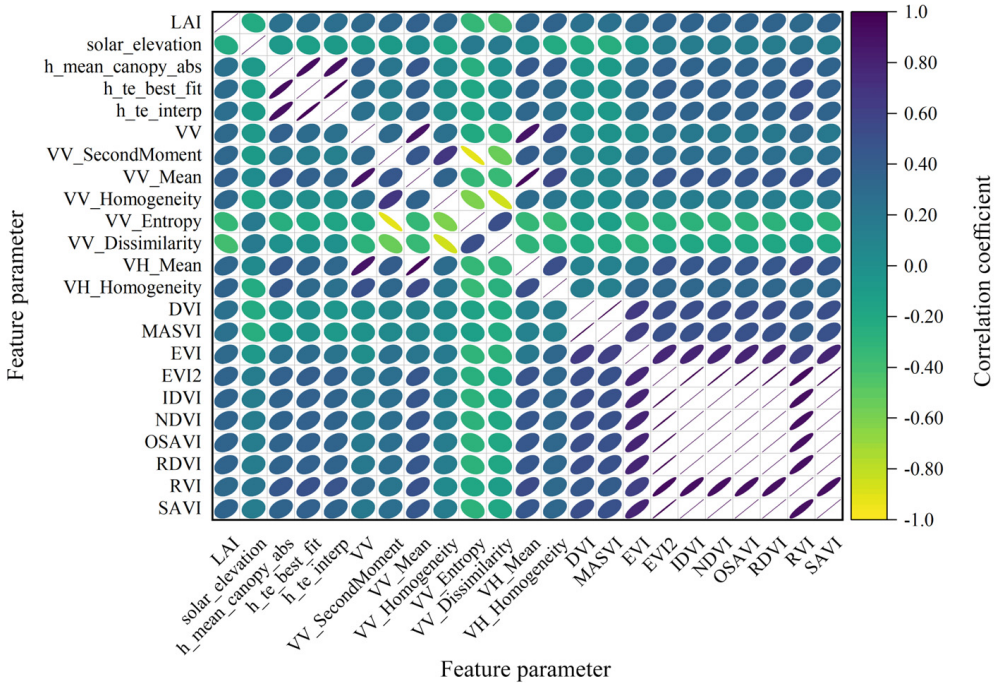

Figure 5. Correlation coefficient thermal matrix diagram.

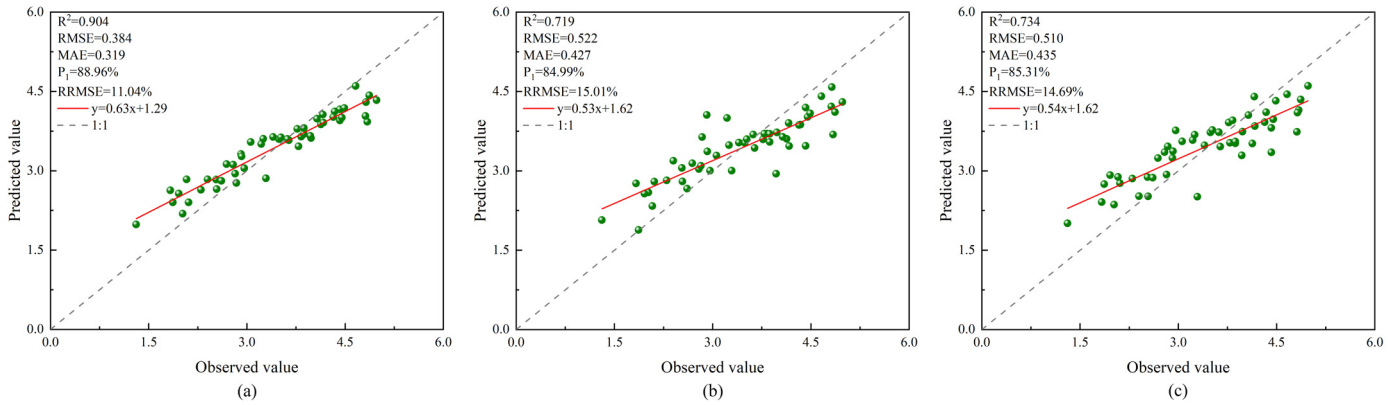

Figure 6. Model fitting scatter plot: (**a**) RF; (**b**) GBRT; and (**c**) KNN.

4.4. Estimation Results of Combined Models of Different Remote Sensing Data Sources

4.4.1. Single ICESat-2/ATLAS Data

To augment the depth of contrast among data source combinations, we have distinctly chosen four parameters—h_te_best_fit, h_te_interp, h_mean_canopy_abs, and solar_elevation—from the ICESat-2/ATLAS dataset as modeling indicators, thereby delineating a singular type of contrast in remote sensing data sources. The findings are illustrated in Figure 7.

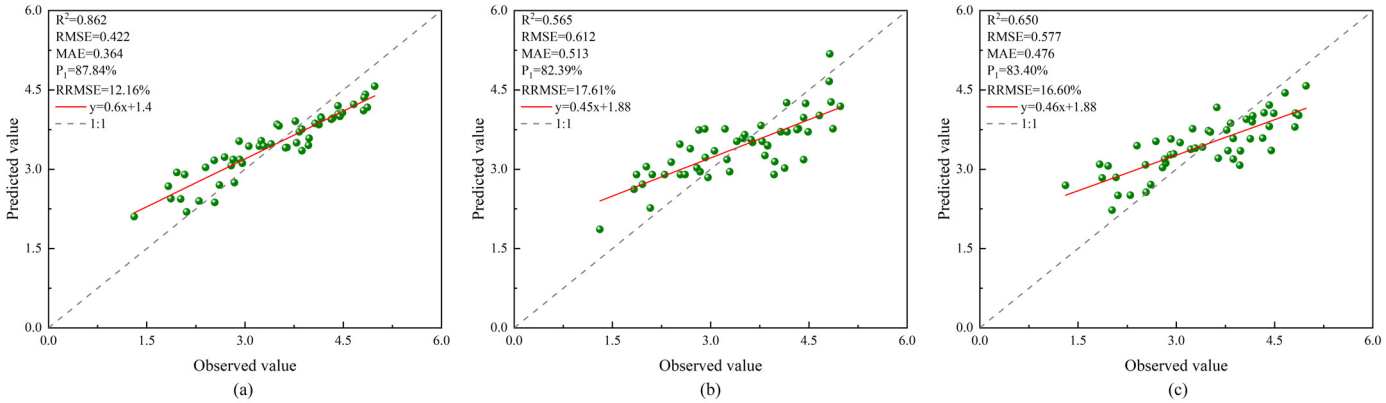

Figure 7. Using only ICESat-2/ATLAS data: (**a**) RF; (**b**) GBRT; and (**c**) KNN.

4.4.2. Combination of Different Remote Sensing Data Sources

- Integration of ICESat-2/ATLAS and Sentinel-1 Data: The study opted for ICESat-2/ATLAS parameters, encompassing h_te_best_fit, h_te_interp, solar_elevation, and h_mean_canopy_abs, in conjunction with Sentinel-1 parameters VV_Mean and VV_Dissimilarity, as indicators for modeling purposes. The model's effects are depicted in Figure 8a–c.

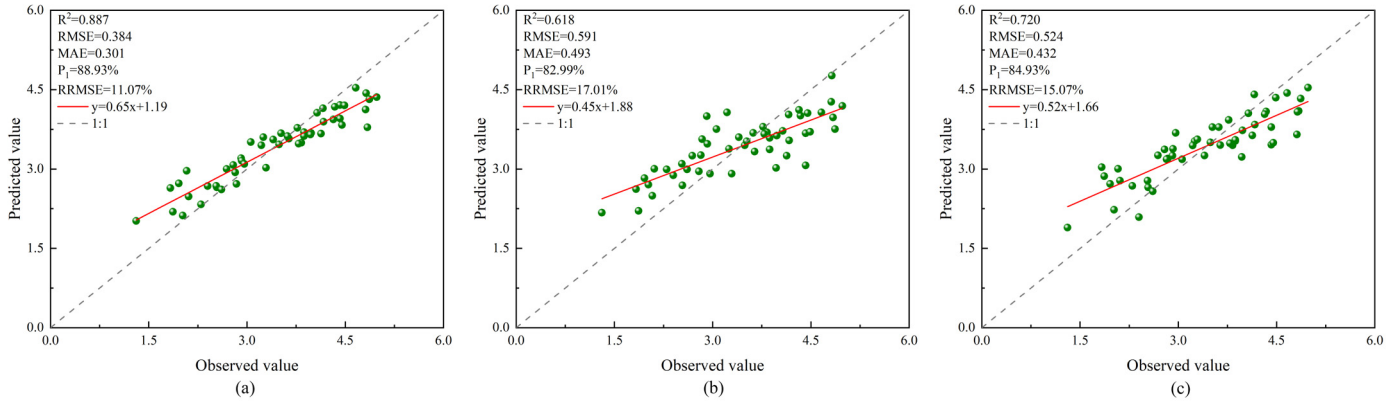

Figure 8. ICESat-2/ATLAS and Sentinel-1 combination: (**a**) RF; (**b**) GBRT; and (**c**) KNN.

- Integration of ICESat-2/ATLAS and Sentinel-2 Data: The study selected parameters from ICE-Sat-2/ATLAS, encompassing h_te_best_fit, h_te_interp, solar_elevation, and h_mean_canopy_abs, in conjunction with Sentinel-2 parameters EVI2 and NDVI, to serve as modeling indicators. The performance of the model is depicted in Figure 9a–c.

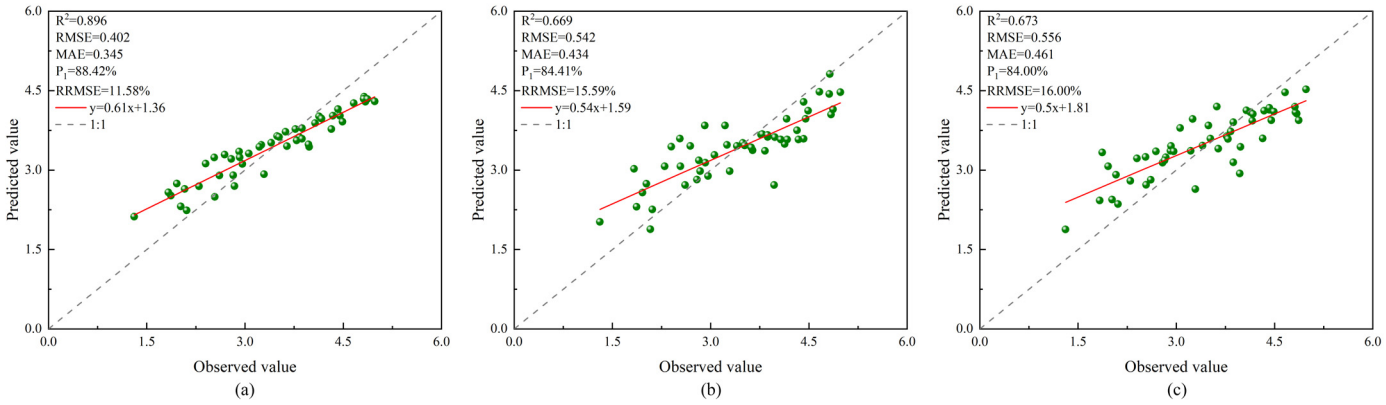

Figure 9. ICESat-2/ATLAS and Sentinel-2 combination: (**a**) RF; (**b**) GBRT; and (**c**) KNN.

4.4.3. Comparison of Model Effects

Models were separately established for single and multiple data sources based on ICESat-2/ATLAS data, and were integrated with various remote sensing data sources. Table 8 illustrates that the RF model, integrating ICESat-2/ATLAS, Sentinel-1, and Sentinel-2 data, showcased the most superior performance, achieving R^2, RMSE, MAE, $P_{1,}$ and RRMSE values of 0.904, 0.384, 0.319, 88.96%, and 11.04%, correspondingly. Among the four data combinations and three models, the RF model exhibited the optimal performance, with the KNN model slightly trailing the RF model, and the GBRT model demonstrating moderate performance. When comparing the RF models constructed using the combination of ICESat-2/ATLAS, Sentinel-1, and Sentinel-2 data with the other three combinations, the performance of the ICESat-2/ATLAS and Sentinel-2 data combination (R^2 = 0.896, RMSE = 0.402, MAE = 0.345, P_1 = 88.42%, RRMSE = 11.58%) was slightly inferior to that of the ICE-Sat-2/ATLAS, Sentinel-1, and Sentinel-2 data combination but superior to that of the ICE-Sat-2/ATLAS and Sentinel-1 data combination (R^2 = 0.887, RMSE = 0.384, MAE = 0.301, P_1 = 88.93%, RRMSE = 11.07%). Nevertheless, the RF model constructed solely with ICESat-2/ATLAS data displayed the lowest performance, recording R^2 of 0.862, RMSE of 0.422, MAE of 0.364, P_1 of 87.84%, and RRMSE of 12.16%. The study demonstrates that the integration of ICESat-2/ATLAS data with other remote sensing datasets for LAI estimation can effectively enhance the accuracy of LAI estimation. Additionally, the combination with various auxiliary datasets also leads to minor fluctuations in model accuracy.

4.5. Spatial Distribution of LAI of Dendrocalamus giganteus in Xinping County

This study employed ICESat-2/ATLAS spaceborne laser altimetry data in conjunction with other optical remote sensing data to estimate the spatial distribution of LAI in Xinping County, employing Sequential Gaussian Conditional Simulation (SGCS) and optimal models. Comparing four different combinations of data sources and employing three machine learning methods, the analysis revealed that the Random Forest (RF) model, utilizing ICESat-2/ATLAS in conjunction with Sentinel-1 and Sentinel-2, produced the most accurate LAI estimations within the study area, as illustrated in Figure 10. This figure unequivocally illustrates the spatial distribution of LAI in *Dendrocalamus giganteus*, demonstrating notable disparities, characterized by an average of 2.4. LAI values predominantly falling within the range of 2.29 to 2.51, wherein the elevated values are discernible, notably in Gasa Town, Laochang Township, and Shuitang Town. Regions characterized by lower LAI values exhibit a scattered and heterogeneous distribution devoid of a distinct and recognizable pattern, possibly influenced by local climatic conditions, soil composition, or other environmental variables.

Table 8. Model accuracy of different data sources.

Parameter Category	Model Parameters	RF Model Accuracy	GBRT Model Accuracy	KNN Model Accuracy
ICESat-2/ATLAS, Sentinel-1, Sentinel-2	h_te_best_fit, h_te_interp, h_mean_canopy_abs, solar_elevation, VV_Mean, VV_Dissimilarity, EVI2, NDVI	R^2 = 0.904 RMSE = 0.384 MAE = 0.319 P_1 = 88.96% RRMSE = 11.04%	R^2 = 0.719 RMSE = 0.522 MAE = 0.427 P_1 = 84.99% RRMSE = 15.01%	R^2 = 0.734 RMSE = 0.510 MAE = 0.435 P_1 = 85.31% RRMSE = 14.69%
ICESat-2/ATLAS	h_te_best_fit, h_te_interp, h_mean_canopy_abs, solar_elevation	R^2 = 0.862 RMSE = 0.422 MAE = 0.364 P_1 = 87.84% RRMSE = 12.16%	R^2 = 0.565 RMSE = 0.612 MAE = 0.513 P_1 = 82.39% RRMSE = 17.61%	R^2 = 0.650 RMSE = 0.577 MAE = 0.476 P_1 = 83.40% RRMSE = 16.60%
ICESat-2/ATLAS, Sentinel-1	h_te_best_fit, h_te_interp, solar_elevation, h_mean_canopy_abs, VV_Mean, VV_Dissimilarity	R^2 = 0.887 RMSE = 0.384 MAE = 0.301 P_1 = 88.93% RRMSE = 11.07%	R^2 = 0.618 RMSE = 0.591 MAE = 0.493 P_1 = 82.99% RRMSE = 17.01%	R^2 = 0.720 RMSE = 0.524 MAE = 0.432 P_1 = 84.93% RRMSE = 15.07%
ICESat-2/ATLAS, Sentinel-2	h_te_best_fit, h_te_interp, h_mean_canopy_abs, solar_elevation, EVI2, NDVI	R^2 = 0.896 RMSE = 0.402 MAE = 0.345 P_1 = 88.42% RRMSE = 11.58%	R^2 = 0.669 RMSE = 0.542 MAE = 0.434 P_1 = 84.41% RRMSE = 15.59%	R^2 = 0.673 RMSE = 0.556 MAE = 0.461 P_1 = 84.00% RRMSE = 16.00%

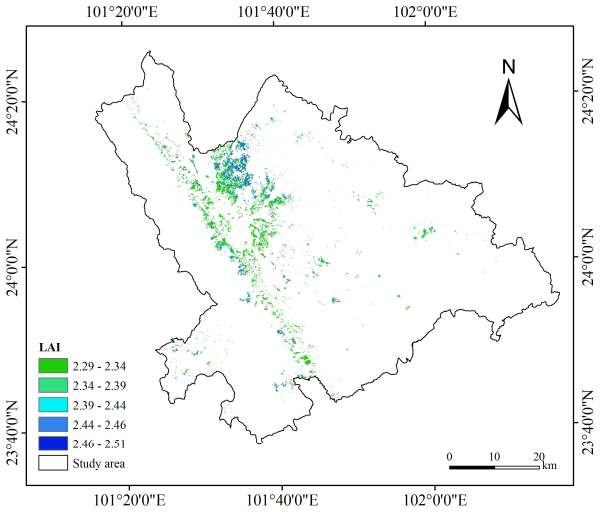

Figure 10. Spatial distribution map of *Dendrocalamus giganteus* LAI in the study area.

5. Discussion

5.1. Selection of Feature Factors

The accuracy of the inversion model and its results are, to a considerable extent, determined by the selection and combination of feature variables [59]. This study employs advanced photon technology LiDAR data to acquire pixel-scale feature variables [9] and utilizes the Pearson correlation coefficient method to select parameters with the highest correlation for modeling purposes. When selecting regional-scale feature parameters in optical remote sensing, the "saturation effect" can significantly influence the data. Among these parameters, single-band reflectance is the most affected, followed by vegetation indices, while texture features are the least affected [60,61]. Specifically, Remote sensing data varied in terms of spectral resolution, spatial resolution, and radiometric resolution, leading to differences in LAI light saturation. Additionally, the surface reflectance of vegetation exhibited varying responses when distinguishing vegetation characteristics. Topographic factors influence the distribution, composition, and growth rates of vegetation, affecting spectral reflectance [62]. Consequently, LAI light saturation changed with variations in

species, species structure, elevation, slope, and aspect [63,64]. Spectral reflectance was typically insensitive to the LAI in dense or highly canopied forests, which reduced the accuracy of LAI estimation [65]. Davi et al. [66] discovered that when LAI values exceeded 3 to 5, the saturation of LAI and remote sensing spectral vegetation indices increased. However, by applying different linear models for each year and species, this relationship was enhanced (R^2 = 0.82, RMSE = 0.86). When the number of auxiliary modeling parameters is controlled at 2, the precision of LAI estimation using the combination of ICESat-2/ATLAS with either Sentinel-1 or Sentinel-2 data exceeds that of using ICESat-2/ATLAS data alone. Furthermore, the inclusion of SAR data in conjunction with ICESat-2/ATLAS and Sentinel-2 data leads to additional enhancement in model precision. Consequently, the incorporation of SAR data can facilitate the fusion of multiple data sources, mitigating spectral saturation issues and thereby improving model estimation accuracy [67].

5.2. Difference in Estimation Accuracy of Different Data Sources

When estimating forest structural parameters, a variety of data sources can be independently or jointly utilized for estimation. The accuracy of predictive models varies depending on the different combinations of data, thereby influencing the estimation results. Currently, LAI estimation based on optical remote sensing data are widely utilized [6]. While single-source remote sensing data can effectively estimate vegetation structural parameters, further investigation is required to compare its accuracy with that of multi-source remote sensing data estimation [64]. Yang et al. [68] demonstrated the precise estimation of non-contiguous forest LAI through the integration of GLAS waveform data and Landsat imagery as auxiliary datasets, thereby validating the utility of Landsat imagery in aiding LAI estimation. Sentinel-2 exhibits comparable LAI estimation capabilities to Landsat 8, albeit with a slight performance advantage. However, when Sentinel-2 and Landsat 8 utilize similar spectral bands, their accuracies are comparable [69]. Optical imagery provided detailed spectral information but was susceptible to light saturation effects. In contrast, SAR could penetrate cloud cover and provide vegetation structure parameters without being affected by light saturation. By combining SAR and optical imagery, the complementary strengths of each data type were leveraged to enhance the accuracy of vegetation structure parameter estimation [70,71]. Moghimi et al. [41] achieved optimal forest above-ground biomass (AGB) estimation by integrating Sentinel-1 and Sentinel-2 data. It was found that this integrated approach outperformed the use of any single dataset. The inclusion of Sentinel-2 data significantly enhanced the AGB estimation accuracy, underscoring the importance of remote sensing data fusion. Wang et al. [72] estimated grassland LAI using Sentinel-1, Sentinel-2, and Landsat 8 data, both individually and in combination. The results demonstrated that the LAI estimation accuracy achieved with the combined data significantly surpassed that achieved with individual datasets, mirroring our findings. However, they did not examine the accuracy of estimating LAI using various combinations of data sources. In our study, combining ICESat-2/ATLAS, Sentinel-1, and Sentinel-2 data resulted in a significant enhancement in LAI estimation accuracy compared to using only ICESat-2/ATLAS data. Furthermore, models constructed using a combination of ICESat-2/ATLAS data with either Sentinel-1 or Sentinel-2 data exhibited superior performance compared to those relying solely on ICESat-2/ATLAS data.

5.3. The Future Expandability of Geostatistical Methods

Utilizing Sequential Gaussian Conditional Simulation methods can effectively leverage ICESat-2 data for extrapolating LAI estimation results. Previous research on the inversion of forest structural parameters using satellite LiDAR data have seen some scholars combining optical remote sensing images to achieve scale extrapolation of the estimation results, thereby obtaining a continuous distribution of forest structural parameter inversion results. For instance, Narine et al. [10] employed ICESat-2 data in conjunction with Landsat 8 optical imagery to scale up AGB inversion outcomes across the entirety of the study area. However, this approach necessitates a high level of predictive accuracy for the estimation

model and encounters challenges including secondary transmission of prediction errors and optical data saturation during the extrapolation process, consequently constraining its applicability. In addressing these concerns, our study undertook a structural analysis relying on the variogram function, conducting SGCS analysis on ATLAS footprint features exhibiting high correlation. This process yielded continuous distributions of data attributes across the study area, subsequently employed in RF to achieve a continuous estimation of forest LAI within the research area. This study not only fully exploited ICESat-2 photon data but also effectively circumvented the introduction of new errors and addressed the optical saturation effect inherent in extrapolating LAI estimation results solely derived from optical remote sensing data by integrating SAR data. Furthermore, this study exclusively employed the SGCS method to interpolate the light spot eigenfactors crucial in LAI modeling, without conducting comparisons with alternative geostatistical approaches. Thus, further investigation is warranted to evaluate the effectiveness of other kriging interpolation techniques, such as synergistic kriging and pan-kriging, in interpolating the light spot eigenvectors.

6. Conclusions

In this study, the geostatistical Variance Function and SGCS methods were employed to extend the LAI estimation of *Dendrocalamus giganteus* from point to polygon in Xinping County, thereby offering novel opportunities and methodologies for applying geostatistics to large-scale forest and bamboo forest LAI estimation. Concurrently, ICESat-2/ATLAS, Sentinel-1, and Sentinel-2 data were integrated for regional-scale LAI estimation. The high vertical resolution of spaceborne lidar compensated for the weather dependency of optical remote sensing images, while SAR's all-weather capability addressed the spatial coverage limitation of spaceborne lidar. This approach effectively enhanced the accuracy of LAI estimation. This study's results demonstrated the significant potential of satellite-borne LiDAR data for LAI estimation. Furthermore, integrating optical remote sensing imagery and SAR data addressed the limitations of individual techniques, thereby enhancing the accuracy of LAI estimation. This approach introduced an innovative method for large-scale LAI estimation utilizing a limited number of sample data points, and proposed a novel framework for large-scale LAI estimation employing multi-source remote sensing data.

Future work could involve exploring other geostatistical methods to interpolate ICESat-2/ATLAS data and integrate them with additional remote sensing datasets, thereby enhancing the accuracy of LAI estimation and producing a high-resolution large-scale LAI spatial distribution map.

Author Contributions: Conceptualization, Q.S., L.X., M.W., and C.X.; Methodology, Z.Q., J.Y., L.X., and M.W.; Software, Z.Q., H.Y., and J.Y.; Validation, Z.Q. and J.Y.; Formal analysis, H.Y., L.X., M.W., and C.X.; Investigation, Z.Q., H.Y., C.X., and D.D.; Resources, Q.S. and D.D.; Writing—original draft, Z.Q.; Writing—review and editing, Q.S.; Supervision, H.Y.; Project administration, Q.S. and D.D.; Funding acquisition, Q.S. and D.D. All authors have read and agreed to the published version of the manuscript.

Funding: This research was funded by the National Key R and D Program of China (No. 2023YFD2201205), the Joint Agricultural Project of Yunnan Province (No. 202301BD070001-002), and the National Natural Science Foundation of China (Nos. 31860205 and 31460194) in 2024.

Data Availability Statement: All remote sensing data used in our research are open source and free of charge. ICESat-2/ATLAS data were acquired from NASA NSIDC (https://search.earthdata.nasa.gov, accessed on 20 January 2024), while Sentinel-1 and Sentinel-2 data were obtained from the GEE platform (https://code.earthengine.google.com, accessed on 20 January 2024).

Acknowledgments: All authors are grateful to NASA and GEE for providing the ICESat-2/ATLAS, Sentinel-1, and Sentinel-2 data. Finally, we sincerely thank the editors and reviewers for their valuable comments.

Conflicts of Interest: The authors declare no conflicts of interest.

References

1. Fang, H.; Baret, F.; Plummer, S.; Schaepman-Strub, G. An overview of global leaf area index (LAI): Methods, products, validation, and applications. *Rev. Geophys.* **2019**, *57*, 739–799. [CrossRef]
2. Chen, J.M.; Black, T. Defining leaf area index for non-flat leaves. *Plant Cell Environ.* **1992**, *15*, 421–429. [CrossRef]
3. Jonckheere, I.; Fleck, S.; Nackaerts, K.; Muys, B.; Coppin, P.; Weiss, M.; Baret, F. Review of methods for in situ leaf area index determination: Part I. Theories, sensors and hemispherical photography. *Agric. For. Meteorol.* **2004**, *121*, 19–35. [CrossRef]
4. Wulder, M.A.; White, J.C.; Stinson, G.; Hilker, T.; Kurz, W.A.; Coops, N.C.; St-Onge, B.; Trofymow, J. Implications of differing input data sources and approaches upon forest carbon stock estimation. *Environ. Monit. Assess.* **2010**, *166*, 543–561. [CrossRef] [PubMed]
5. Yan, G.; Hu, R.; Luo, J.; Weiss, M.; Jiang, H.; Mu, X.; Xie, D.; Zhang, W. Review of indirect optical measurements of leaf area index: Recent advances, challenges, and perspectives. *Agric. For. Meteorol.* **2019**, *265*, 390–411. [CrossRef]
6. Fang, H. Retrieval of forest vertical leaf area index and clumping index through field measurement and remote sensing techniques: A review. *Chin. Sci. Bull.* **2021**, *66*, 3141–3153. [CrossRef]
7. Lefsky, M.A.; Cohen, W.B.; Parker, G.G.; Harding, D.J. Lidar remote sensing for ecosystem studies: Lidar, an emerging remote sensing technology that directly measures the three-dimensional distribution of plant canopies, can accurately estimate vegetation structural attributes and should be of particular interest to forest, landscape, and global ecologists. *BioScience* **2002**, *52*, 19–30.
8. Brunt, K.M.; Neumann, T.A.; Walsh, K.M.; Markus, T. Determination of local slope on the Greenland Ice Sheet using a multibeam photon-counting Lidar in preparation for the ICESat-2 Mission. *IEEE Geosci. Remote Sens. Lett.* **2013**, *11*, 935–939. [CrossRef]
9. Zhu, X. Forest Height Retrieval of China with a Resolution of 30 m Using ICESat-2 and GEDI Data. Ph.D. Thesis, Aerospace Information Research Institute, Chinese Cademy of Sciences, Beijing, China, 2021.
10. Narine, L.L.; Popescu, S.C.; Malambo, L. Using ICESat-2 to estimate and map forest aboveground biomass: A first example. *Remote Sens.* **2020**, *12*, 1824. [CrossRef]
11. Yang, Z.; Shu, Q.; Qiu, S.; Xi, L. Regional-scale forest LAI estimation based on ICESat-2/ATLAS data combined with Kriging interpolation. *J. Yunnan Univ. (Nat. Sci. Ed.)* **2023**, *45*, 1157–1170.
12. Teng, J. Carbon Storage and Energy of Typical Sympodial Bamboo Ecosystems in China. Master's Thesis, Zhejiang A and F University, Hangzhou, China, 2016.
13. Ji, J.; Li, X.; Du, H.; Mao, F.; Fan, W.; Xu, Y.; Huang, Z.; Wang, J.; Kang, F. Multiscale leaf area index assimilation for Moso bamboo forest based on Sentinel-2 and MODIS data. *Int. J. Appl. Earth Obs. Geoinf.* **2021**, *104*, 102519. [CrossRef]
14. Wang, C.; Huang, M.; Wnag, W.; Li, Z.; Zhang, T.; Ma, L.; Bai, Y.; Wang, Y.; Shi, J.; Long, R.; et al. Variation characteristics of plant community diversity and above-ground biomass in alpine degraded slopes along altitude gradients in the headwaters region of three-river on Tibetan plateau. *Acta Ecol. Sin.* **2022**, *42*, 3640–3655.
15. Li, M.; Li, Y.; Zhao, W.; Wang, J. Characteristics and Geographical Distribution of Ancient Tree Groups in Xinping County. *For. Inventory Plan.* **2023**, *48*, 153–160.
16. Zeng, Y.; Li, J.; Liu, Q.; Hu, R.; Mu, X.; Fan, W.; Xu, B.; Yin, G.; Wu, S. Extracting leaf area index by sunlit foliage component from downward-looking digital photography under clear-sky conditions. *Remote Sens.* **2015**, *7*, 13410–13435. [CrossRef]
17. Markus, T.; Neumann, T.; Martino, A.; Abdalati, W.; Brunt, K.; Csatho, B.; Farrell, S.; Fricker, H.; Gardner, A.; Harding, D. The Ice, Cloud, and land Elevation Satellite-2 (ICESat-2): Science requirements, concept, and implementation. *Remote Sens. Environ.* **2017**, *190*, 260–273. [CrossRef]
18. Xie, D.; Li, G.; Wang, J.; Guo, J.; Me, J.; Yang, C. An Overview of the Application Prospect of New Laser Altimetry Satellite ICESat-2 in Geoscience. *Geomat. Spat. Inf. Technol.* **2020**, *43*, 38–42+45.
19. Torres, R.; Snoeij, P.; Geudtner, D.; Bibby, D.; Davidson, M.; Attema, E.; Potin, P.; Rommen, B.; Floury, N.; Brown, M. GMES Sentinel-1 mission. *Remote Sens. Environ.* **2012**, *120*, 9–24. [CrossRef]
20. Drusch, M.; Del Bello, U.; Carlier, S.; Colin, O.; Fernandez, V.; Gascon, F.; Hoersch, B.; Isola, C.; Laberinti, P.; Martimort, P. Sentinel-2: ESA's optical high-resolution mission for GMES operational services. *Remote Sens. Environ.* **2012**, *120*, 25–36. [CrossRef]
21. Phiri, D.; Simwanda, M.; Salekin, S.; Nyirenda, V.R.; Murayama, Y.; Ranagalage, M. Sentinel-2 data for land cover/use mapping: A review. *Remote Sens.* **2020**, *12*, 2291. [CrossRef]
22. WANG, M.; Fan, C.; GAO, B.; REN, Z.; LI, F. A spatial random forest interpolation method with semi-variogram. *Chin. J. Eco-Agric.* **2022**, *30*, 451–457.
23. Hock, B.; Payn, T.; Shirley, J. Using a geographic information system and geostatistics to estimate site index of Pinus radiata for Kaingaroa Forest, New Zealand. *New Zealand J. For. Sci.* **1993**, *23*, 264–277.
24. Berterretche, M.; Hudak, A.T.; Cohen, W.B.; Maiersperger, T.K.; Gower, S.T.; Dungan, J. Comparison of regression and geostatistical methods for mapping Leaf Area Index (LAI) with Landsat ETM+ data over a boreal forest. *Remote Sens. Environ.* **2005**, *96*, 49–61. [CrossRef]
25. Emery, X.; Peláez, M. Assessing the accuracy of sequential Gaussian simulation and cosimulation. *Comput. Geosci.* **2011**, *15*, 673–689. [CrossRef]
26. Zhao, Y.; Hua, Q.; Chen, J. Comparison of kriging interpolation with conditional sequential Gaussian simulation in principles and case analysis of their application in study on soil spatial variation. *Acta Pedofil. Sin.* **2011**, *48*, 856–862.
27. Matheron, G. Les variables régionalisées et leur estimation: Une application de la théorie de fonctions aléatoires aux sciences de la nature. 1965. Available online: https://cir.nii.ac.jp/crid/1130282273252256768 (accessed on 15 January 2024).

28. Zhang, S.; Shao, M.; Li, D. Prediction of soil moisture scarcity using sequential Gaussian simulation in an arid region of China. *Geoderma* **2017**, *295*, 119–128. [CrossRef]
29. Qu, M.; Li, W.; Zhang, C. Spatial distribution and uncertainty assessment of potential ecological risks of heavy metals in soil using sequential Gaussian simulation. *Hum. Ecol. Risk Assess. Int. J.* **2014**, *20*, 764–778. [CrossRef]
30. Huang, J.; Liu, W.; Zeng, G.; Li, F.; Huang, X.; Gu, Y.; Shi, L.; Shi, Y.; Wan, J. An exploration of spatial human health risk assessment of soil toxic metals under different land uses using sequential indicator simulation. *Ecotoxicol. Environ. Saf.* **2016**, *129*, 199–209. [CrossRef] [PubMed]
31. Olea, R.A.; Pawlowsky, V. Compensating for estimation smoothing in kriging. *Math. Geol.* **1996**, *28*, 407–417. [CrossRef]
32. Zhao, Y.; Sun, Z.; Chen, J. Analysis and Comparison in Arithmetic for Kriging Interpolation and Sequential Gaussian Conditional Simula-tion. *J. Geo-Inf. Sci.* **2010**, *12*, 767–776.
33. Luo, S.; Xu, L.; Yu, J.; Zhou, W.; Yang, Z.; Wang, S.; Guo, C.; Gao, Y.; Xiao, J.; Shu, Q. Sampling Estimation and Optimization of Typical Forest Biomass Based on Sequential Gaussian Conditional Simulation. *Forests* **2023**, *14*, 1792. [CrossRef]
34. Breiman, L. Random forests. *Mach. Learn.* **2001**, *45*, 5–32. [CrossRef]
35. Zhang, W.; Tang, L.; Chen, F.; Yang, J. Prediction for TBM Penetration Rate Using Four Hyperparameter Optimization Methods and Random Forest Model. *J. Basic Sci. Eng.* **2021**, *29*, 1186–1200. [CrossRef]
36. Friedman, J.H. Greedy function approximation: A gradient boosting machine. *Ann. Stat.* **2001**, 1189–1232. [CrossRef]
37. Friedman, J.H. Stochastic gradient boosting. *Comput. Stat. Data Anal.* **2002**, *38*, 367–378. [CrossRef]
38. Scheuber, M. Potentials and limits of the k-nearest-neighbour method for regionalising sample-based data in forestry. *Eur. J. For. Res.* **2010**, *129*, 825–832. [CrossRef]
39. Ver Hoef, J.M.; Temesgen, H. A comparison of the spatial linear model to nearest neighbor (k-NN) methods for forestry applications. *PLoS ONE* **2013**, *8*, e59129. [CrossRef] [PubMed]
40. Gjertsen, A.K. Accuracy of forest mapping based on Landsat TM data and a kNN-based method. *Remote Sens. Environ.* **2007**, *110*, 420–430. [CrossRef]
41. Moghimi, A.; Darestani, A.T.; Mostofi, N.; Fathi, M.; Amani, M. Improving forest above-ground biomass estimation using genetic-based feature selection from Sentinel-1 and Sentinel-2 data (case study of the Noor forest area in Iran). *Kuwait J. Sci.* **2024**, *51*, 100159. [CrossRef]
42. Cai, W.; Zhao, S.; Wang, Y.; Peng, F. Estimation of winter wheat residue cover using spectral and textural information from Sentinel-2 data. *Natl. Remote Sens. Bull.* **2020**, *24*, 1108–1119. [CrossRef]
43. Chen, B.; Pang, Y.; Li, Z.; North, P.; Rosette, J.; Sun, G.; Suárez, J.; Bye, I.; Lu, H. Potential of forest parameter estimation using metrics from photon counting LiDAR data in Howland Research Forest. *Remote Sens.* **2019**, *11*, 856. [CrossRef]
44. Ghosh, S.M.; Behera, M.D.; Paramanik, S. Canopy height estimation using sentinel series images through machine learning models in a mangrove forest. *Remote Sens.* **2020**, *12*, 1519. [CrossRef]
45. Jiang, F.; Sun, H.; Li, C.; Ma, K.; Chen, S.; Long, J.; Ren, L. Retrieving the forest aboveground biomass by combining the red edge bands of Sentinel-2 and GF-6. *Acta Ecol. Sin* **2021**, *41*, 8222–8236.
46. Wu, G.; Fang, Y.; Jiang, Q.; Cui, M.; Li, N.; Ou, Y.; Diao, Z.; Zhang, B. Early identification of strawberry leaves disease utilizing hyperspectral imaging combing with spectral features, multiple vegetation indices and textural features. *Comput. Electron. Agric.* **2023**, *204*, 107553. [CrossRef]
47. Rouse, J. Monitoring the Vernal Advancement and Retrogradation of Natural Vegetation. NASA/GSFCT Type II Report. 1973. Available online: https://cir.nii.ac.jp/crid/1570291224983494528 (accessed on 15 January 2024).
48. Clevers, J. The application of a vegetation index in correcting the infrared reflectance for soil background. In Proceedings of the Symposium on Remote Sensing for Research and Development in Environmental Management, Enschede, The Netherlands, 21–24 April 1986; pp. 221–226.
49. Huete, A.R. A soil-adjusted vegetation index (SAVI). *Remote Sens. Environ.* **1988**, *25*, 295–309. [CrossRef]
50. Rondeaux, G.; Steven, M.; Baret, F. Optimization of soil-adjusted vegetation indices. *Remote Sens. Environ.* **1996**, *55*, 95–107. [CrossRef]
51. Huete, A.; Didan, K.; Miura, T.; Rodriguez, E.P.; Gao, X.; Ferreira, L.G. Overview of the radiometric and biophysical performance of the MODIS vegetation indices. *Remote Sens. Environ.* **2002**, *83*, 195–213. [CrossRef]
52. Jiang, Z.; Huete, A.R.; Didan, K.; Miura, T. Development of a two-band enhanced vegetation index without a blue band. *Remote Sens. Environ.* **2008**, *112*, 3833–3845. [CrossRef]
53. Pearson, R.L.; Miller, L.D. Remote mapping of standing crop biomass for estimation of the productivity of the shortgrass prairie, Pawnee National Grasslands, Colorado. In Proceedings of the Eighth International Symposium on Remote Sensing of Environment, Ann Arbor, MI, USA, 2–6 October 1972.
54. Qi, J.; Chehbouni, A.; Huete, A.R.; Kerr, Y.H.; Sorooshian, S. A modified soil adjusted vegetation index. *Remote Sens. Environ.* **1994**, *48*, 119–126. [CrossRef]
55. Gitelson, A.A.; Merzlyak, M.N. Remote sensing of chlorophyll concentration in higher plant leaves. *Adv. Space Res.* **1998**, *22*, 689–692. [CrossRef]
56. Rouse, J.W.; Haas, R.H.; Schell, J.A.; Deering, D.W. Monitoring vegetation systems in the Great Plains with ERTS. *NASA Spec. Publ* **1974**, *351*, 309.

57. Rouse Jr, J.W.; Haas, R.H.; Deering, D.; Schell, J.; Harlan, J.C. Monitoring the Vernal Advancement and Retrogradation (Green Wave Effect) of Natural Vegetation. 1974. Available online: https://ntrs.nasa.gov/citations/19750020419 (accessed on 15 January 2024).
58. Xu, C.; Pu, L.; Zhu, M.; XU, C.; Zhang, M.; Xu, Y. Prediction of Soil Heavy Metals Content Based on Sequential Gaussian Simulation and Evaluation of Its Uncertainties: A Case Study of Soil Hg Content in Yixing. *Acta Pedol. Sin.* **2018**, *55*, 999–1006.
59. Zhang, W.; Zhao, L.; Li, Y.; Shi, J.; Yan, M.; Ji, Y. Forest Above-Ground Biomass Inversion Using Optical and SAR Images Based on a Multi-Step Feature Optimized Inversion Model. *Remote Sens.* **2022**, *14*, 1608. [CrossRef]
60. Zhao, P.; Lu, D.; Wang, G.; Wu, C.; Huang, Y.; Yu, S. Examining spectral reflectance saturation in Landsat imagery and corresponding solutions to improve forest aboveground biomass estimation. *Remote Sens.* **2016**, *8*, 469. [CrossRef]
61. Shu, Q.; Xi, L.; Wang, K.; Xie, F.; Pang, Y.; Song, H. Optimization of samples for remote sensing estimation of forest aboveground biomass at the regional scale. *Remote Sens.* **2022**, *14*, 4187. [CrossRef]
62. Feng, X.; Tan, S.; Dong, Y.; Zhang, X.; Xu, J.; Zhong, L.; Yu, L. Mapping large-scale bamboo forest based on phenology and morphology features. *Remote Sens.* **2023**, *15*, 515. [CrossRef]
63. Luo, T.; Neilson, R.P.; Tian, H.; Vörösmarty, C.J.; Zhu, H.; Liu, S. A model for seasonality and distribution of leaf area index of forests and its application to China. *J. Veg. Sci.* **2002**, *13*, 817–830. [CrossRef]
64. Wu, J.; Chen, P.; Fu, S.; Chen, Q.; Pan, X. Co-inversion of island leaf area index combination morphological and spectral parameters based on UAV multi-source remote sensing data. *Ecol. Inform.* **2023**, *77*, 102190. [CrossRef]
65. Mutanga, O.; Masenyama, A.; Sibanda, M.J.I.J.o.P.; Sensing, R. Spectral saturation in the remote sensing of high-density vegetation traits: A systematic review of progress, challenges, and prospects. *ISPRS J. Photogramm. Remote Sens.* **2023**, *198*, 297–309. [CrossRef]
66. Davi, H.; Soudani, K.; Deckx, T.; Dufrene, E.; Le Dantec, V.; Francois, C. Estimation of forest leaf area index from SPOT imagery using NDVI distribution over forest stands. *Int. J. Remote Sens.* **2006**, *27*, 885–902. [CrossRef]
67. Zhou, W.; Shu, Q.; Wang, S.; Yang, Z.; Luo, S.; Xu, L.; Xiao, J. Estimation of forest canopy closure in northwest Yunnan based on multi-source remote sensing data colla-boration. *Chin. J. Appl. Ecol.* **2023**, *34*, 1806–1816. [CrossRef]
68. Yang, X.; Wang, C.; Pan, F.; Nie, S.; Xi, X.; Luo, S. Retrieving leaf area index in discontinuous forest using ICESat/GLAS full-waveform data based on gap fraction model. *ISPRS J. Photogramm. Remote Sens.* **2019**, *148*, 54–62. [CrossRef]
69. Korhonen, L.; Packalen, P.; Rautiainen, M. Comparison of Sentinel-2 and Landsat 8 in the estimation of boreal forest canopy cover and leaf area index. *Remote Sens. Environ.* **2017**, *195*, 259–274. [CrossRef]
70. Stankevich, S.A.; Kozlova, A.A.; Piestova, I.O.; Lubskyi, M.S. Leaf area index estimation of forest using sentinel-1 C-band SAR data. In Proceedings of the 2017 IEEE Microwaves, Radar and Remote Sensing Symposium (MRRS), Kiev, Ukraine, 29–31 August 2017; pp. 253–256.
71. Rosso, P.; Nendel, C.; Gilardi, N.; Udroiu, C.; Chlebowski, F. Processing of remote sensing information to retrieve leaf area index in barley: A comparison of methods. *Precis. Agric.* **2022**, *23*, 1449–1472. [CrossRef]
72. Wang, J.; Xiao, X.; Bajgain, R.; Starks, P.; Steiner, J.; Doughty, R.B.; Chang, Q. Estimating leaf area index and aboveground biomass of grazing pastures using Sentinel-1, Sentinel-2 and Landsat images. *ISPRS J. Photogramm. Remote Sens.* **2019**, *154*, 189–201. [CrossRef]

Disclaimer/Publisher's Note: The statements, opinions and data contained in all publications are solely those of the individual author(s) and contributor(s) and not of MDPI and/or the editor(s). MDPI and/or the editor(s) disclaim responsibility for any injury to people or property resulting from any ideas, methods, instructions or products referred to in the content.